Measurements of Ocean Surface Backscattering Using an Airborne 94-GHz Cloud Radar – Implication for Calibration of Airborne and Spaceborne W-band Radars

LIHUA LI

Goddard Earth Sciences and Technology Center, University of Maryland, Baltimore, Maryland

GERALD M. HEYMSFIELD

NASA Goddard Space Flight Center, Greenbelt, Maryland

LIN TIAN

Goddard Earth Sciences and Technology Center, University of Maryland, Baltimore, Maryland

PAUL E. RACETTE

NASA Goddard Space Flight Center, Greenbelt, Maryland

April 27, 2004

To be submitted to the Journal of Atmospheric and Oceanic Technology

---

Corresponding author address: Lihua Li, NASA Goddard Space Flight Center, Code 912, Building 33, Room C426, Greenbelt, MD 20771.
E-mail: lihua@agnes.gsfc.nasa.gov

ABSTRACT

Backscattering properties of the ocean surface have been widely used as a calibration reference for airborne and spaceborne microwave sensors. However, at millimeter-wave frequencies, the ocean surface backscattering mechanism is still not well understood, in part, due to the lack of experimental measurements. During the Cirrus Regional Study of Tropical Anvils and Cirrus Layers-Florida Area Cirrus Experiment (CRYSTAL-FACE), measurements of ocean surface backscattering were made using a 94-GHz (W-band) cloud radar onboard a NASA ER-2 high-altitude aircraft. The measurement set includes the normalized ocean surface cross section over a range of the incidence angles under a variety of wind conditions. Analysis of the radar measurements shows good agreement with a quasi-specular scattering model. This unprecedented dataset enhances our knowledge about the ocean surface scattering mechanism at 94 GHz. The results of this work support the proposition of using the ocean surface as a calibration reference for airborne millimeter-wave cloud radars and for the ongoing NASA CloudSat mission, which will use a 94-GHz spaceborne cloud radar for global cloud measurements.

1. Introduction

Clouds play a critical role in the Earth's climate system. The vertical structure and spatial distributions of clouds are important in determining the Earth's radiation budgets, which affect global circulations and ultimately climate. However, the lack of fine-scale cloud data is apparent in current climate model simulations (Houghton et al. 1995; Stephens et al. 1990). In cloud detection, millimeter-wave cloud radars have gained favor because of their high scattering efficiency, low power consumption, and compact size. A number of airborne millimeter-wave cloud radars have been developed (Pazmany et al. 1994; Sadowy et al. 1997; Li et al. 2003). Meanwhile, a 94-GHz spaceborne cloud radar is in preparation for the NASA CloudSat program (Stephens et al. 2002). Another proposed spaceborne W-band cloud radar is the joint Japanese/European Earth Cloud, Aerosol and Radiation Explorer (EarthCARE) mission radar, as described by the European Space Agency (2001).

One challenge of using millimeter-wave radar for measuring clouds is achieving system calibration. The delicate nature of millimeter-wave components and the harsh environment in which they operate may cause undetected changes in the system response unless regular system calibration is performed. The calibration uncertainty specification of the CloudSat 94 GHz cloud radar is 2 dB (with a goal of 1.5 dB) (Stephens et al. 2002). Typically, a radar may utilize internal circuitry to monitor the variation of the power levels of the radio frequency (RF) transmitter and the drift of system gain, but characterization of the antenna, front-end waveguides, and the interfaces between these components, are not included with internal calibration. External calibrations using point targets, such as a trihedral corner reflector, have been performed for ground-based radars (Li et al. 2003; Sekelsky 2002). However, it is difficult to calibrate airborne or spaceborne radars using

point targets due to the difficulty in separating the return of the calibration reference from background clutter.

The ocean surface has been widely used as a calibration target for airborne and spaceborne microwave radars and radiometers. Numerous studies of ocean surface scattering have been performed at microwave frequencies (Jones et al. 1976; Plant 1977; Valenzuela 1978; Masuko et al. 1986). Based on experiences with operating millimeter-wave cloud radars on the ground and on airborne platforms, it will be essential to perform CloudSat radar calibration checks periodically once it is launched. The ocean surface will be a valuable calibration reference since there will be many measurement opportunities under clear-sky conditions. However, in part because of the lack of experimental measurements at millimeter-wave frequencies, the ocean surface backscattering mechanism is still not well understood. Meanwhile, attenuation caused by water-vapor and oxygen absorption in the lower troposphere is significant at millimeter-wave frequencies. It is therefore necessary to correct this attenuation to reduce the uncertainty of the calibration. In addition to the radar calibration, the ocean surface return can also be used in estimating the path- integrated attenuation (PIA) along the radar beam. The PIA then is used as a constraint for retrieving radar attenuation, rain rate, or cloud particle microphysical properties (Meneghini et al. 1983; Iguchi and Meneghini 1994).

During July 2002, the Cloud Radar System (CRS), a 94-GHz (W-band) pulsed-Doppler polarimetrc radar developed by NASA Goddard Space Flight Center, was operated on a NASA ER-2 high-altitude (nominal 20 km) research aircraft in support of the NASA CRYSTAL-FACE program (Jensen et al. 2003). During the same experiment, the 9.6-GHz ER-2 Doppler Radar (EDOP) (Heymsfield et al. 1996), dropsondes (Hock and Franklin 1999) as well as other remote

sensors were also operated on the ER-2. Table 1 shows CRS system parameters during CRYSTAL-FACE. The radar calibration was performed using a trihedral corner reflector after the CRYSTAL-FACE . The calibration result was verified by side-by-side inter-comparison with the University of Massachusetts (UMass) ground-based Cloud Profiling Radar System (CPRS) 95-GHz cloud radar (Sekelsky and McIntosh 1996), which has been well maintained and calibrated over the past decade. Inter-comparison measurements between the CRS and CPRS for similar cloud volumes were conducted during autumn 2002. Figure 1 shows a comparison of CRS and CPRS W-band radar reflectivity profiles. The mean difference of the profiles in clouds is within 1 dB. The details of the CRS hardware, installation on ER-2, system calibration, and preliminary cloud measurements from CRYSTAL-FACE are described by Li et al. (2003) and McGill et al. (2003).

During the CRYSTAL-FACE, the ocean surface backscattering was measured by CRS over the southern Florida offshore region. The radar measurements are used to investigate the efficacy of using ocean surface returns as a reference for calibrating airborne and spaceborne W-band radars. This paper presents a comparative analysis of the CRS CRYSTAL-FACE data with an ocean surface backscatter model using three parameterizations of the mean surface slope. In Section 2 the ocean surface backscatter model is introduced, and the dependency of the ocean surface radar cross section on incidence angle and surface wind speed is discussed. The need to correct for atmospheric attenuation at 94 GHz is discussed as well. Section 3 explains configuration of the instrumentation during the CRYSTAL-FACE and describes the dataset used in this study. Section 4 presents CRS measurements and compares these measurements with EDOP data and the backscatters models.

2. Background

a. Ocean surface backscatter model

In general, the normalized ocean surface scattering cross section σ_o is a function of radar wavelength, radar beam incidence angle, polarization, ocean surface wind speed, and wind direction. For incidence angle θ smaller than 15°, σ_o is dominated by large-scale surface waves, and at microwave frequencies the quasi-specular scattering theory has been shown to work well in this region (Valenzuela 1978; Barrick 1974; Brown 1990). When θ is larger than 15°, Bragg scattering produced by small-scale waves becomes more significant, and therefore, two-scale scatter models have been used since they take into account both quasi-specular scattering and Bragg scattering (Brown 1978; Chan and Fung 1977). For the CRS operating on the NASA ER-2 and for the CloudSat radar, the primary measurement objective is to obtain vertical profiles of cloud and precipitation layers. Therefore, these radars are designed to operate at low incidence angles and the quasi-specular scattering theory is considered valid. Under this theory, the ocean surface is assumed isotropic and the surface wave distribution probability density is only a function of the surface mean-square slope, $s(v)$; σ_o is then approximately given as (Valenzuela 1978; Brown 1990):

$$\sigma_o(\theta, v, \lambda) = \frac{|\Gamma_e(0,\lambda)|^2}{s(v)^2 \cos^4(\theta)} \exp\left(-\frac{\tan^2(\theta)}{s(v)^2}\right), \quad (1)$$

where λ is the radar wavelength, v is surface wind speed in ms^{-1}, and $s(v)^2$ is the effective mean-square surface slope. The ocean surface effective Fresnel reflection coefficient at normal incidence, $\Gamma_e(0,\lambda) = C_e(n(\lambda)\text{-}1.0)/(n(\lambda)+1.0)$, and $n(\lambda)$ is the complex refractive index for seawater. For the CRS operating frequency, $n(\lambda = 3mm) = 3.36\text{-}j1.93$ at 20 C (Meneghini and Kozu 1990). The

Fresnel reflection coefficient correction factor, C_e, will be discussed in Section 3c. It is worth noting that this quasi-specular can not resolve the dependency of σ_o on wind direction.

The effective mean-square surface slope, $s(v)^2$, is given by different empirical relationships. Cox and Munk (1954) developed a linear relationship based on classical optical scattering data. They showed that $s(v)^2 = 0.003+5.08\text{x}10^{-3}v$, varied linearly with wind speed for both a low-pass filtered surface where only gravity waves are present, and a "clean" surface which includes capillary wave scale roughness. Wu (1972, 1990) reanalyzed the data obtained by Cox and Munk (1954) and showed that the mean-square slope varies approximately with the logarithm of wind speed. Therefore, $s(v)^2$ is expressed as $s(v)^2 = w_0+w_1 log_{10}(v)$, where w_0 and w_1 are empirically determined constants, but different in two wind speed regimes: for $v < 7.0$ ms^{-1}, $w_0 = 0.009$ and $w_1 = 0.0276$; for $7.0 < v < 20.0$ ms^{-1}, $w_0 = -0.084$ and $w_1 = 0.138$. Based on the statistical analysis of the σ_o measurements obtained by the Tropical Rainfall Measuring Mission (TRMM) K_u-band (13.8-GHz) precipitation radar and surface wind measurements obtained by the passive TRMM Microwave Imager, Frelich and Vanhoff (2003) derived $w_0 = 0.0036$ and $w_1 = 0.028$ for $1.0 < v < 10.0$ ms^{-1}, and $w_0 = -0.0184$ and $w_1 = 0.05$ for $10.0 < v < 20.0$ ms^{-1}. In the following, these three surface slope relationships are discussed and compared with radar measurements from CRYSTAL-FACE.

Figure 2a shows σ_o at 94 GHz versus incidence angle at 2.0, 6.0 and 10.0 ms^{-1} wind speed using the above three different $s(v)^2$ empirical relationships. In general, as the surface wind speed increases, the surface roughness increases and the shape of the σ_o versus incidence angle curve becomes flatter. At a given wind speed, σ_o calculated using TRMM $s(v)^2$ decreases more rapidly with the increase of incidence angle. For 10.0 ms^{-1} wind, the results from Cox and Munk (1954),

and Wu (1972, 1990) are basically identical, so that these two curves are indistinguishable in Fig. 2a. Although the σ_o versus θ relationships are different for the three different empirical models, the difference tends to be the smallest near a 10^o incidence angle.

Figure 2b gives σ_o versus wind speed at 5^o, 10^o, and 15^o incidence angles for different $s(v)^2$ empirical relationships. For $5.0 < v < 18.0$ ms^{-1}, σ_o calculated using Cox and Munk's (1954) and Wu's (1972, 1990) $s(v)^2$ relationships are nearly the same at all three incidence angles except for a 1 dB discrepancy near 7.0 ms^{-1} at 5^o and 15^o incidence angles. This is due to the discontinuity in Wu's relationship at a 7.0 ms^{-1} wind speed. It is worth noting that σ_o is less sensitive to wind speed near a 10^o incidence angle for all three $s(v)^2$ relationships when wind speed is higher than 2 ms^{-1}. This has been reported by many authors from previous measurements using microwave radars (Jones et al. 1976; Plant 1977; Masuko et al. 1986). In addition, Figure 2b also indicates that at a 10^o incidence angle, σ_o estimates using the three different $s(v)^2$ empirical relationships agree within 1 dB for $3.0 < v < 10.0$ ms^{-1}. This fact is very useful for calibration of airborne or spaceborne radars since pointing the radar beam at incidence angles near 10^o over an ocean surface minimizes uncertainties due to surface wind variations.

b. Radar equation of ocean surface scattering

The basic form of a radar equation for surface scatter is given by (Kozu 1995):

$$P_r = \frac{10^6 P_t G_a{}^2 \lambda^2 \sigma_o \beta\varphi \cos(\theta)}{512 \ln 2 \pi^2 l_r l_{tx} l_{atm}{}^2 h^2}, \tag{2}$$

where, P_r = power at the receiver (mW),

P_t = peak transmit power (kW),

G_a = antenna gain,

λ = radar signal wavelength (m),

β, φ = antenna 3 dB beamwidth in horizontal and vertical (radians),

l_r = loss between the antenna and receiver port,

l_{tx} = loss between the transmitter and the antenna port,

l_{atm}= one-way path-integrated atmospheric attenuation

θ = radar beam incidence angle (radians),

σ_o = normalized ocean surface radar cross section, and

h = altitude of the aircraft (m).

The product of $\frac{P_t G_a^{\,2} \lambda^2 \beta \varphi}{l_r l_{tx}}$ only depends on the radar system parameters. This product is related to the radar constant such as that used by Sekelsky (2002),

$$R_c = \frac{1024 \ln 2 \lambda^2 l_{tx} l_r 10^{21}}{P_t G_a^{\,2} c \pi^3 \tau \beta \varphi}, \tag{3}$$

where c is the speed of light (3×10^8 ms^{-1}), and τ is the RF pulse width (s).

R_c can be evaluated from: 1) measurements of individual parameters in (3); 2) an external calibration using a target with known radar cross section, such as a trihedral corner reflector (Sekelsky 2002); and 3) the ocean surface. For our case, R_c for the CRS was obtained from a series of external calibrations using a trihedral corner reflector (Li et al. 2003) as mentioned earlier. Assuming that a beam-filled condition is satisfied, σ_o can be calculated as

$$\sigma_o = \frac{P_r c \pi^5 l_{atm}{}^2 \tau R_c h^2}{2\lambda^4 10^{21} \cos(\theta)}. \quad (4)$$

On the other hand, if the ocean surface conditions and σ_o are known, the radar constant can be derived from (4) so that radar calibration is achieved. In Section 4, observational estimates of σ_o and their dependence on the radar beam incidence angle and surface wind conditions are examined.

c. Attenuation due to atmospheric absorption

Water vapor and oxygen molecules do not produce significant backscatter at 94 GHz. However, water-vapor and oxygen absorption at millimeter-wave frequencies is much stronger than at microwave frequencies (Lhermitte 1988; Clothiaux et al. 1995; Li et al. 2001). Because water vapor and oxygen are highly concentrated in the lower troposphere, ocean surface measurements made from an airborne or spaceborne radar are attenuated by their presence. For tropical and mid-latitude regions the attenuation can be significant. In subtropical ocean areas such as Florida, the two-way path-integrated attenuation from water-vapor and oxygen absorption can be as high as 7 dB as a result of the high humidity and high temperature. A practical atmospheric millimeter-wave propagation model developed by Liebe (1985) predicts attenuation and path delay of moist air for frequencies up to 1000 GHz. The input variables of this model are height distributions (0-30 km) of pressure, temperature, and humidity along the propagation path. Using profiles of relative humidity, temperature, and pressure measured by the ER-2 dropsondes and radiosondes launched from the surface, the attenuation has been estimated and corrected using Liebe's (1985) millimeter-wave propagation model.

3. Data description and processing

a. Radar configuration during CRYSTAL-FACE

During CRYSTAL-FACE, the CRS was installed in the tail cone of the ER-2 right wing superpod, while EDOP was operated from the nose of the ER-2. The measurement geometry of the CRS during the CRYSTAL-FACE experiment is illustrated in Fig. 3. Since the CRS was configured in a fixed nadir pointing mode, incidence angle scanning in the cross-track direction was achieved when the ER-2 made routine maneuvers. When the ER-2 changed its flight direction, it rolled its body to one side and gradually changed its heading direction, then rolled back to a level position to complete the turn. The incidence angle of the radar beam, θ, is derived using aircraft pitch-and-roll angles.

The CRS antenna has an elliptical beam with a beamwidth of 0.6^o crosstrack and 0.8^o alongtrack. The ER-2 flew at a nominal 20-km altitude; therefore the CRS footprint size on the surface is 210 m cross track and 280 m along track. The RF pulse width of the CRS was 1.0 μs (150 m in range), and data were averaged for 0.5 s before being stored onto a solid-state recorder. With the 1.0 μs pulse width, the surface footprint is beam-filled up to a 32^o incidence angle. During the CRYSTAL-FACE flights, the maximum radar beam incidence angle was less than 30^o when the aircraft made turns. Therefore, all CRS measurements from this experiment were valid for the beam-filled condition. Meanwhile, the CRS data were sampled at a 0.25-μs time interval (37.5-m range spacing), and the ocean surface return was oversampled by a factor of four. Oversampling the surface return is a technique used for airborne and satellite observations which significantly reduces the error of the surface return power (Kozu 2000; Caylor et al. 1997).

The incidence angles of the CRS radar beam are determined using aircraft pitch-and-roll angles, which are provided by the aircraft navigation system at an 8-Hz rate and simultaneously recorded along with the 2-Hz radar data. The accuracy of the aircraft pitch and roll is 0.05^{o}. Ideally, the radar beam should be pointed along nadir. However, during installation, alignment errors result in offsets of the radar beam from nadir in both pitch and roll. These offsets are estimated and corrected using σ_o and Doppler velocity measurements of the ocean surface. The offset in pitch (along track) was obtained using the Doppler velocity of the ocean surface, which should be 0 ms^{-1} on average. Using this method, the CRS antenna pointing uncertainty was determined to be about 0.2^{o} in pitch. The offset in roll (cross track) was estimated by comparing σ_o measurements from right and left turns. At low incidence angles, σ_o versus θ curves measured from right and left turns should agree with each other since σ_o is not sensitive to wind direction at low incidence angles (Jones et al. 1976). The CRS beam offset in roll was determined to be less than 0.4^{o} (see Section 4a and Fig. 10).

In this study, measurements of σ_o made by CRS are compared to the measurements made by the 9.6-GHz EDOP, which has two beams, one pointing to nadir and the other pointing to 33^{o} forward from nadir. The EDOP has been well calibrated using the TRMM precipitation radar and ocean surface return (Heymsfield et al. 1996, 2000). The beamwidth of the EDOP nadir beam antenna is 2.9^{o}, about four times that of the CRS beamwidth. The RF pulse width and sampled gate spacing of EDOP are 0.5 μs (75 m in range) and 37.5 m, respectively. For this operating mode, the beam filled approximation is only valid for incidence angles smaller than 5^{o}. Therefore, σ_o measured by the EDOP nadir beam is calculated using "partially beam-filled" equation (Equation [16] in Kozu [1995]) so that it is comparable to the CRS data. In order to reduce the errors in the measurement of σ_o, EDOP ocean surface return was oversampled by a factor of two.

b. Atmospheric attenuation estimation and surface wind speed

Sounding data profiles, used to estimate atmospheric attenuation, were obtained by the ER-2 GPS dropsondes (RD-93 model) developed by the National Center for Atmospheric Research (NCAR) (Hock and Franklin 1999). They provided pressure, temperature, humidity, and surface horizontal wind, etc. The measurement accuracies of these dropsondes are: pressure, ±1.0 hPa; temperature ±0.2 C; humidity, ±7%; horizontal wind, ±0.1 ms^{-1}. During the CRYSTAL-FACE, between 4 and 8 dropsondes were typically launched during each 5-hour flight. Figure 4 shows temperature, relative humidity, and pressure profiles measured by a dropsonde from clear-sky conditions at 1954 UTC, 9 July 2002. The latitude and longitude of the dropsonde launch point were N23.83^o and W86.15^o, respectively. The estimated two-way integrated attenuation due to water-vapor and oxygen absorption is shown in Fig. 4d. For this case, the maximum two-way attenuation due to water-vapor and oxygen absorption is 6.7 dB.

The ER-2 flew 11 science missions during the experiment in which about 50 dropsondes were launched. Figure 5a shows the two-way path-integrated attenuation due to water-vapor and oxygen absorption under clear weather condition. The results show that the averaged two-way integrated water-vapor and oxygen attenuation is approximately 5.8 dB with a standard deviation of 0.55 dB. The high attenuation and large standard deviation reveal the importance of the correction of ocean surface measurements for atmospheric attenuation. In addition to the near-surface measurements made by the dropsondes, ocean surface wind measurements were obtained from nearby surface buoys as well. Figure 5b shows the surface wind speed measured by ER-2

dropsondes during CRYSTAL-FACE. The measurements indicate that the ocean surface wind speed was between 1 and 7 ms^{-1} for most ER-2 flights.

c. Estimate of correction factor C_e

For a smooth surface, the Fresnel reflection coefficient at normal incidence is given by the classic formula as $\Gamma(0,\lambda) = (n(\lambda)-1.0)/(n(\lambda)+1.0)$, where $n(\lambda)$ is the complex refractive index of the surface materials (Ulaby et al. 1981). At 94 GHz, $n(\lambda = 3mm) = 3.36\text{-}j1.93$ for 20 C seawater (Meneghini and Kozu 1990); therefore, $|\Gamma(0, \lambda = 3mm)|^2 = 0.409$ for a smooth ocean surface. However, the ocean surface is generally roughened by gravity waves, surface winds, and precipitation. According to Jackson et al. (1992), small-scale surface roughness diffracts the incident radiation. This diffractive process reduces the Fresnel reflection coefficient. It is therefore necessary to use effective Fresnel reflection coefficient $\Gamma_e(0, \lambda) = C_e(n(\lambda) -1.0)/(n(\lambda)+1.0)$, where C_e accounts for the surface roughness effects. C_e is generally smaller than 1 and is equal to 1 only for a perfectly smooth surface.

Based on the statistical analysis of the ocean surface backscattering measurements obtained by the Tropical Rainfall Measuring Mission K_u-band (13.8 GHz) spaceborne radar, Frelich and Vanhoff (2003) estimated that C_e is approximately 0.89 for surface wind speed between 1.5 ms^{-1} and 15 ms^{-1}. At 94 GHz, estimates of C_e have been difficult to obtain due to the lack of measurements of the ocean surface. Here, we compare σ_o calculated from (1) and σ_o measured by the CRS to estimate C_e. At low incidence angle (near nadir), σ_o is not useful for estimating C_e because it is sensitive to different $s(v)^2$ empirical relationships (see Fig. 2) and has relatively large variability with surface wind speed at nadir. However, at a 10^o incidence angle, σ_o is insensitive to

surface wind speed and to $s(v)^2$ empirical relationships for $3.0 < v < 10.0$ ms^{-1}. The mean value of σ_o calculated within this wind speed range ($3.0 < v < 10.0$ ms^{-1}) for all three $s(v)^2$ relationships is $6.94 + 20\log(C_e)$ dB. σ_o measurements at 10^o incidence angles obtained by the CRS from different turn events have a mean value of 5.85 dB and a standard deviation of 0.6 dB. Since σ_o calculated from the model should agree with the measurement, C_e is then estimated as 0.88 with an uncertainty of 0.16. Errors in system calibration, σ_o calculation, and atmospheric attenuation estimates are possible sources of the uncertainty in C_e. This C_e estimate is almost the same as the TRMM estimate, but it does not necessarily mean that C_e is frequency independent. More experimental data are necessary to examine the dependency of C_e on radar frequencies.

4. σ_o observed by the CRS

a. σ_o versus incidence angle

On 9 July 2002, the ER-2 flew a tropical cirrus mission from its base at Key West, Florida, through the Yucatan Channel, then south-southeast into the Caribbean Sea (Fig. 6). On the return trip, the ER-2 made a turn through point B (1935 UTC, N21.72^o, W86.11^o) under clear weather. Figure 7 shows the aircraft navigation data, incidence angle, and surface return power. It indicates that the ER-2 rolled its body to the right side during the first half of the turn, and rolled back in the second half of the turn to resume a level position. During the turns, the CRS radar beam scanned along the cross-track direction away from and back to nadir. Figure 8 shows σ_o measured by CRS versus the incidence angle compared with theoretical curves. The σ_o measured by EDOP is also shown in Fig. 8 as diamonds. Figure 8 shows a larger variation in EDOP measurements, which were oversampled by a factor of two than the CRS measurements, which was over sampled by a factor of four. This observation is consistent with the results reported by Caylor et al. (1997) and

Kozu et al. (1995), and indicates that the errors in σ_o estimates can be reduced by oversampling along the radar range.

It is difficult to obtain the exact surface wind conditions at turn point B, but measurements were made by dropsondes launched at 1601 UTC (N23.75^o, W86.16^o), and at 1644 UTC (N19.01^o, W86.91^o) on the outbound trip, and at 1954 UTC (N23.83^o, W86.16^o) on the return trip (see locations in Fig 6). The near surface wind speeds measured by these dropsondes were 2.6 ms^{-1}, 3.1 ms^{-1}, and 6.8 ms^{-1}, respectively. Results using the models described in Section 2 with wind speeds of 2.5 ms^{-1}, 3.0 ms^{-1} and 6.5 ms^{-1} are plotted for comparison in Fig. 8. In Fig. 8a, the CRS measurements fall between the 2.5 ms^{-1} and 6.5 ms^{-1} Cox and Munk model predictions, and they are closest to the 3.0 ms^{-1} curve. However, near a 10^o incidence angle, the CRS measurements (~ 6 dB) agree well with the model results for the three wind speeds. For EDOP, only the 3.0 ms^{-1} Cox and Munk model result is plotted (dashed-dotted line. Fig. 8a). Figure 8b shows that both the CRS and EDOP measurements match well with Wu's (1990) surface slope relationship for 3.0 ms^{-1} wind speed up to 12^o incidence angle. For incidence angles larger than 12^o, Bragg scattering produced by small-scale waves becomes more significant, and thus, two-scale models have to be used (Barrick 1974; Brown 1978). Similarly, Fig. 8c shows radar measurements and model results using the surface slope relationship from TRMM data. For the same surface wind speed, TRMM's surface slope relationship predicts higher σ_o for low incidence angle (<10^o), and more rapid decrease of σ_o along with an increase of the incidence angle. For this case, radar measurements are closest to the 6.5 ms^{-1} curve.

On 26 July 2002, the ER-2 flew a similar flight pattern to the Caribbean sea as on 9 July. Figure 9 shows a portion of the flight track near two directional turns, with an insert of the full

flight pattern. The aircraft flew an almost identical track on the outbound and return trips. Similar to Fig. 8, Fig. 10 shows σ_o versus incidence angle during the turns close to way point F. For the outbound trip, the ER-2 flew through E, F, and G at 1721 UTC, and σ_o is shown in Fig. 10 as "+" . During the return trip, the ER-2 flew through G, F, and E at 1956 UTC, and the corresponding curve is presented by "◊" in Fig. 10. Surface wind speed measured by dropsonde was 2.5 ms^{-1} at 1753 UTC (N18.51^o, W84.48^o), and 2.3 ms^{-1} at 2017 UTC (N24.0^o, W86.15^o). The quasi-specular models using different surface slope relationships with 2.5 ms^{-1} surface wind speed are shown by the curves in Fig. 10. It is evident that radar measurements from the outbound turn and return trip turn agree very well even though they were two-and-half hours apart in time. At a low incidence angle, radar measurements match well with model results and are in closer agreement with Wu's (1972, 1990) relationship than the other two. It is worth noting that although the models are "tuned" using $C_{e,}$ which is estimated from CRS measurements, the shape of σ_o versus θ curve will not be affected by possible errors in C_e since these errors only result in offsets in the σ_o.

Other turn events from different days of the experiment were also used to calculate σ_o as a function of incidence angle. Figure 11 shows σ_o versus incidence angle from 12 clear weather cases. Each case is indicated by a different letter. The different dependencies of σ_o with incidence angle are due to the difference in ocean surface structure attributed to different surface winds. Results from the quasispecular model with three different surface slope relationships and with 1.25 ms^{-1} and 8.0 ms^{-1} wind speeds, are plotted for comparison. It is noteworthy that near the 10^o incidence angle, σ_o measurements are less sensitive to wind speed, which also agrees with the quasi-specular model and measurements obtained at lower microwave frequencies (Jones et al. 1976; Plant 1977; Masuko et al. 1986). As discussed in Section 4c, σ_o at 10^o incidence angle were

obtained from turn events, during which surface winds were within 3.0-10.0 ms^{-1}. The mean value of the measured σ_o is 5.85 dB with a standard deviation of 0.6 dB.

b. Effects of wind speed and direction on σ_o

Figure 12 presents measured σ_o at 3^o, 10^o, and 15^o incidence angles versus ocean surface wind speed. Results using the quasispecular model and three different surface slope relationships are also shown for comparison. The discrepancy between the radar measurements and model results is likely due to: a) the uncertainty of the wind speed estimate caused by a collocation error between the radar beam footprint on the ocean surface and the dropsonde fall position at the surface; b) an error in the estimates of the water vapor and oxygen attenuation; c) possible errors in the model.

Measurements at microwave frequencies have shown that not only the wind speed, but also the wind direction and polarization of the radar beam affect scattering from the ocean surface. Jones et al. (1976) showed that σ_o were slightly different for upwind, downwind and crosswind conditions at a low incidence angle. However, this difference becomes more significant when incidence angles are larger than 15^o. During CRYSTAL-FACE, the CRS transmit polarization was such that the E-field was perpendicular to the direction of flight, thereby, the radar signal was vertically polarized (V-plane) relative to the ocean surface during the turns.

For the 26 July case shown above, the ER-2 made nearly a right angle turn at 1700 UTC during the outbound flight (through A, B, C and D in Fig. 9). A dropsonde, launched at 2117 UTC on the return trip, measured a surface wind speed of 2.3 ms^{-1} from 211^o. Figure 13 presents σ_o versus incidence angle during the turn. The radar beam was oriented upward and slightly to the right of the wind in the first half turn (shown by "+" in Fig. 13) and then changed over to the left of

the wind in the second half of the turn (shown by "◊" in Fig. 13). For an incidence angle larger than 12 ^{o}, the discrepancy of σ_o between the first half and second half of the turn is evident.

From 1731:38 to 1734:29 UTC on 29 July 2002, the ER-2 performed a 250^{o} clockwise turn in azimuth while maintaining a constant roll (~25^{o}) and incidence angle (~29^{o}). Figure 15 shows σ_o versus the ER-2 heading angle from this turn. The nearest available buoy (FWYF1 at N25.59^{o} W80.10^{o}) measured a 3.3 ms^{-1} wind 57^{o} from the north. The radar beam scanned in the cross-track plane which was 90^{o} from the ER-2 heading. Therefore, the radar beam was pointing approximately upwind when the ER-2 heading angle was 227^{o}. As evident in Fig. 14, σ_o reached its maximum when the radar beam was close to upwind and a minimum when the radar beam was pointing in the crosswind direction. These observations are in general agreement with the measurements made by Jones et al. (1976) at 13.9 GHz. Note that the offset between the σ_o maximum and the upwind direction is likely due to a small wind-direction error since the buoy was about 22 km away from the center of the turn.

c. Comparison of ocean and land surface return

The CRS-measured surface returns were highly variable over different surface conditions (topography, vegetation, etc.). Compared to terrestrial topography, the ocean surface is more homogeneous, and thus the ocean surface return is less variable. Figure 15 shows an ER-2 flight leg (2022:49 to 2122:25 UTC) on 13 July 2002 covering ocean and land backgrounds, while Fig. 16 shows the measured sea surface σ_o between points A and C of this line (2056 to 2112 UTC). Between points A (2056:46 UTC) and point B (2104:53 UTC), where the ER-2 was flying over the ocean, the standard deviation of σ_o is about 0.307 dB; The standard deviation for the inland flight

portion (point B to point C) is 3.12 dB. This significant increase in the standard deviation of σ_o is due to the irregularity of the topography and possibly speckle reflection from natural or man- made objects. Since we know that the radar beam incidence angle did not vary significantly during the flight path, the transition point between ocean and land can be found by examining the standard deviation of σ_o measurements. By combining this information with navigational data, the radar beam pointing angle in the along-track plane at the ocean/land crossing point then can be estimated. One of the practical applications of this method is to determine the approximate pointing direction of the beam for a spaceborne cloud radar.

5. Conclusion

In this paper, we have examined the possibility of using the ocean surface as a calibration reference for airborne and spaceborne millimeter-wave cloud radars. During the CRYSTAL-FACE experiment, ocean surface backscattering measurements were obtained using the 94-GHz CRS airborne cloud radar, which was calibrated on the ground using a trihedral corner reflector and by intercomparing measurements with another well-calibrated ground-based radar (Li et al. 2003). The uncertainty of this ground-based calibration is estimated to be 1 dB. This calibration was then applied to deriving estimates of the normalized ocean surface backscatter cross section σ_o from the surface return. Attenuation due to water-vapor and oxygen absorption is estimated and corrected using a Liebe millimeter-wave propagation model and the meteorological data collected by the ER-2 dropsondes.

In our study, the σ_o measured by the CRS is compared with a quasi-specular ocean surface scattering model using different surface slope relationships. The analysis results show good

agreement between the theoretical models and the measurements. It was confirmed that even at 94 GHz, the quasi-specular ocean surface scattering model works well for a near-nadir operational mode. The CRS measurements also confirm that the σ_o is insensitive to surface wind conditions near a 10^o incidence angle, a finding similar to what has been found in the literature for lower frequencies. In addition, the CRS measurements show that the dependence of σ_o on surface wind direction is in general agreement with the measurements made at lower microwave frequencies. However, more measurements at 94 GHz are necessary to study the details of this dependence. Moreover, the comparison between the ocean and inland surface returns suggests that the position of the coastline can be accurately determined, which, in turn, can be used for resolving the pointing direction of a spaceborne cloud radar. The analyses in this paper support the proposition of using the ocean surface as a calibration reference for airborne and spaceborne millimeter-wave cloud radars.

When applying a quasi-specular model to the calibration of airborne or spaceborne cloud radars, errors may result from the uncertainties in the water-vapor and oxygen attenuation correction, surface wind measurements, and sampling of the surface return. In addition, the effective Fresnel reflection coefficient $\Gamma_e(0,\lambda)$, instead of $\Gamma(0,\lambda)$, has to be used to account for the effects of surface roughness. Since the CRS was calibrated and the calibration results were verified using different approaches (Li et al. 2003), this enables us to estimate the correction factor C_e using σ_o measured by the CRS during the CRYSTAL-FACE. In our study, C_e is estimated as 0.88 with an uncertainty of 0.16, which corresponds to 1.6 dB in the σ_o calculation (1.0 dB due to the radar calibration, and 0.6 dB in σ_o measurements). Using this C_e and the quasi-specular model, a 2.2 dB calibration uncertainty is achievable for a spaceborne radar using its σ_o measurements at a 10^o incidence angle (a 1.6 dB uncertainty in the C_e estimate and also assuming 0.6 dB uncertainty in σ_o

measurements from the spaceborne radar). More experimental data, such as measurements of backscatter from the ocean surface or wave tank using well-calibrated 94 GHz radars, is necessary to verify the value of C_e for different geographic locations and surface wind conditions, and to reduce the uncertainty in the C_e estimate. It is worth noting that even though C_e is used by the quasi-specular model to estimate σ_o, the shape of σ_o versus θ curve will not be affected by possible errors in C_e since these errors result only in offsets in σ_o.

Acknowledgments: The CRS measurements during the CRSYSTAL-FACE experiment were supported by the NASA CRSYSTAL-FACE Program by Dr. Don Anderson at NASA Headquarters. Thanks to Ed Zenker and Dr. Steve Bidwell for their help in the CRYSTAL-FACE field effort, to the NASA ER-2 crew and pilots for their support during the CRS installation, test flight and field experiment, to Dr. Steve Sekelsky and Eric Knapp of UMass for their help during the CRS/CPRS inter-comparison, to Dr. Jeffrey Halverson for providing ER-2 dropsonde data, and to Dr. Robert Meneghini for instructive discussions.

REFERENCES

Barrick, D. E., 1974: Wind dependence of quasi-specular microwave sea scatter. *IEEE Trans. Antennas and Propag.,* AP-**22**, 135–136.

Brown, G., 1978: Backscattering from a Gaussian-distributited perfectly conducting rough surface. *IEEE Trans. Antennas Propag.,* AP**26**, 472–482.

———, 1990: Quasi-specular scattering from the air-sea interface. *Surface Waves and Fluxes*, Vol. **2**, W. Plant and G. Geernart, Eds., Kluwer Academic, 1–40.

Caylor, I. J., G. M. Heymsfield, R. Meneghini, L. S. Miller, 1997: Correction of sampling errors in ocean surface cross-sectional estimates from nadir-looking weather radar. *J. Atmos. Ocean. Technol.,* **13**, 203–210.

Clothiaux, E., M. Miller, B. Albrecht, T. Ackerman, J. Verlinde, D. Babb, R. Peters, and W. Syrett, 1995: An evaluation of a 94-Ghz radar for radar remote sensing of cloud properties. *J. Atmos. Ocean. Technol.,* **12**, 201–229.

Chan, H. L. and A. K. Fung, 1977: A theory of sea scatter at large incident angle, *J. Geophys. Res.*, **82**, 3439–3444.

Cox, C. and W. Munk, 1954: Measurements of the roughness of the sea surface from photographs of the sun's glitter. *J. Opt. Soci. Amer.,* **144**, 838–850.

European Space Agency, 2001: EarthCARE-Earth Clouds, Aerosols and Radiation Explorer. Rep. for Assessment, The Five Candidate Earth Explorer Core Missions, SP-1257(1), ESA Publication Division, Noordwijk, Netherlands, 135 pp.

Frelich, M. H. and B. A. Vanhoff, 2003: The relationship between winds, surface roughness, and radar backscatter at low incidence angles from TRMM precipitation radar measurements. *J. Atmos. Ocean. Technol.,* **20**, 549–562.

Heymsfield, G. M., S. W. Bidwell, I. J. Caylor, A. S., S. Nicholson, W. C. Boncyk, L. Miller, D. Vandemark, P. E. Racette, and L. R. Dod, 1996: The EDOP radar system on the high-altitude NASA ER-2 aircraft. *J. Atmos. Ocean. Technol.,* **13**, 795–809.

————, B. Geerts and L. Tian, 2000: TRMM precipitation radar reflectivity profiles as compared with high-resolution airborne and ground-based radar measurements. *J. Appli. Meteor.,* **39**, 280–2102.

Hock, T. F. and J. L. Franklin, 1999: The NCAR GPS dropsonde. *Bull. Amer. Meteor. Soc.*, **80**, 407–420.

Houghton, J. T., L. G. Meira, B. A. Callander, N. Harris, A. Katenberg, and K. Maskell, 1995: *Climate Changes 1995-The Science of Climate Change*. Cambridge University Press.

Iguchi, T. and R. Meneghini, 1994: Intercomparison of single-frequency methods for retrieving a vertical rain profile from airborne or spaceborne radar data. *J. Atmos. Ocean. Technol.*, **11**, 1507–1516.

Jackson, F. C., W. T. Walton, and D. E. Hines, 1992: Sea surface mean square slope from K_u-band backscatter data. *J. Geophys. Res.*, **97**, 11411–11427.

Jensen, E.J., D.E. Anderson, H.B. Selkirk, D.O. Starr,and O.B. Toon, 2003: Overview of the Cirrus Regional Study of Tropical Anvils and Cirrus Layers – Florida Area Cirrus Experiment (CRYSTAL-FACE), *Bull. Amer. Meteor. Soci.*, submitted.

Jones, W. L., L. C. Schroeder, and J. L. Michell, 1976: Aircraft measurements of the microwave scattering signature of the ocean. *IEEE Trans. Antennas Propag.,* **25**, 52–61.

Kozu, T., 1995: A generalized surface echo radar equation for down-looking pencil beam radar. *IEICE Trans. Comm.,* **E78-B**, 1245–1248.

———, S. Satoh, H. Hanado, T. Manabe, M. Okumura, K. Okamoto, T. Kawanishi, 2000: Onboard surface detection algorithm from TRMM precipitation radar. *IEICE Trans. Comm.,* **E83-B**, 2021–2031.

Lhermitte R., 1988: Cloud and precipitation remote sensing at 94 GHz. *IEEE Trans. Geosci. Remote Sens.*, **26**(3), 1069–1089.

Li L., S. M. Sekelsky, S. C. Reising , C. T. Swift, S. L. Durden, G. A. Sadowy, S. J. Dinardo, F. K. Li, A. Huffman, G. Stephens, D. M. Babb and H. W. Rosenberger, 2001: Retrieval of

atmospheric attenuation using combined ground-based and airborne 95-GHz cloud radar measurements. *J. Atmos. Ocean. Technol.*, **18**, 1345–53.

———, G. M. Heymsfield, P. E. Racette, L. Tian, and E. Zenker, 2003: An airborne 94-GHz cloud radar on a NASA ER-2. *J. Atmos. Ocean. Technol.*, accepted .

Liebe, H., 1985: An updated model for millimeter-wave propagation in moist air. *Radio Sci.* **20**, 1069–1089.

Masuko, H., K. Okamoto, M. Shimada, and S. Niwa, 1986: Measurements of microwave backscattering signatures of the ocean surface using X-band and Ka band airborne scatterometers. *J. Geophys. Res.,* **91**, 13065–13083.

McGill, M. J., L. Li, W. D. Hart, G. M. Heymsfield, D. L. Hlavka, R. E. Racette, L. Tian, M. A. Vaughan, and D. M. Winker, 2003: Combined lidar-radar remote sensing: Initial results from CRYSTAL-FACE. *J. Geophys. Res.,* accepted.

Meneghini, R., J. Eckerman, and D. Atlas, 1983: Determination of rain rate from a spaceborne radar using measurements of total attenuation. *IEEE Trans. Geosci. Remote Sens.,* **21**, 34–43.

———— and T. Kozu, 1990: *Spaceborne Weather Radar*, Artech House, 199pp.

Pazmany, A. L., R. E. McIntosh, R. Kelly, and G. Vali, 1994: An airborne 95-GHz dual polarization radar for cloud studies. *IEEE Trans. Geosci. Remote Sens.*, **1**, 731–739.

Plant, W. J., 1977: Studies of backscatter sea return with a CW, dual-frequency, X-band radar. *IEEE Trans. Antennas Propag.,* AP**25**, 28–36.

Sadowy, G., R. McIntosh, S. Dinardo, S. Durden, W. Edelstein, F. Li, A. Tanner, W. Wilson, T. Schneider, and G. Stephens, 1997: The NASA DC-8 airborne cloud radar: Design and

preliminary results. *International Geoscience and Remote Sensing Symposium*, Singapore, **4**, 1466–1469.

Sekelsky, S. M. and R. E. McIntosh, 1996: Cloud observations with polarimetrc 33 GHz and 95 GHz radar. *Meteor. and Atmos. Phys.*, **59**, 123-140.

————, 2002: Near field reflectivity and antenna boresight gain corrections for millimeter-wave atmospheric radars. *J. Atmos. Ocean. Technol.,* **19**, 468–477.

Stephens, G. L., S. C. Tsay, P. W. Stackhouse, and P. J. Flatau, 1990: The relevance of the microphysical and radiative properties of cirrus clouds to climate and climate feedback. *J. Atmos. Sci.,* **47**, 1742–1752.

————, D. G. Vane, G. G. Boian, R. J. and Mace, K. Sassen, Z. Wang, A. J. Illingworth, E. J. O'Connor, W. B. Rossow, S. L. Durden, S. D. Miller, R. T. Austin, A. Benedetti, C. Mitrescu, and the CloudSat Science Team, 2002: The CloudSat mission and the A-train. *Bull. Amer. Meteor. Soc.*, **83**, 1771–1789.

Ulaby, F., R. Moore, and A. Fung, 1981: *Microwave Remote Sensing*; *Active and Passive* vol. **1**. Artech House, pp456.

Valenzuela, G. R., 1978: Theories for the interaction of electromagnetic and oceanic waves - a review. *Bound.-Layer Meteor.,* **13**, 61–85.

Wu J., 1972: Sea-surface slope and equilibrium wind-wave spectra. *Phys. Fluids*, **15**, 741–747.

———, 1990: Mean square slopes of the wind disturbed water surface, their magnitude, directionality, and composition. *Radio Sci.*, **25**, 37–48.

List of Figures

Figure 9. ER-2 flight track on 26 July 2002. A larger scope plot is shown at the upper left-hand corner. ER-2 flew the track on its outbound trip and on its return trip. It made turns at way points B and F.

Figure 10. σ_o measured by the CRS versus incidence angle from the turns near way point F shown in Fig. 8. Cross represents for measurements from the outbound turn through E, F, and G consequentially. Diamond represents measurements from the turn through G, F, and E on the return trip consequentially.

Figure 11. σ_o measured by the CRS versus incidence angle from different days. A total of 12 turns from clear weather is shown.

Figure 12. σ_o versus ocean surface wind speed at different incidence angle. Results from the quasi-specular scattering model are shown as the solid, dotted and dashed lines.

Figure 13. σ_o from a turn with 100^o heading change. It indicates that σ_o varies relative to wind direction for incidence angle larger than 12^o.

Figure 14. σ_o versus ER-2 heading angle.

Figure 15. ER-2 flight track on 13 July 2002. It crossed the coastline at point B (21:04:53 UTC).

Figure 16. σ_o measured by the CRS from 20:56 to 21:12 UTC. From the ocean to inland, it shows significant increase in the standard deviation of σ_o.

TABLE 1: CRS system specifications during CRYSTAL-FACE

Frequency (GHz)	94.155
Peak power (kW)	1.7
PRF (kHz)	4/5 (Dual PRF)
Pulse width (μs)	1.0
Transmit polarization	H
Receive polarization	V and H
Antenna beamwidth (^{o})	0.6x0.8
Antenna gain (dB)	46.4
Sensitivity (dBZe) *	-29 (from flight data),

* At 10-km range, 150-m range resolution, 1-sec averaging

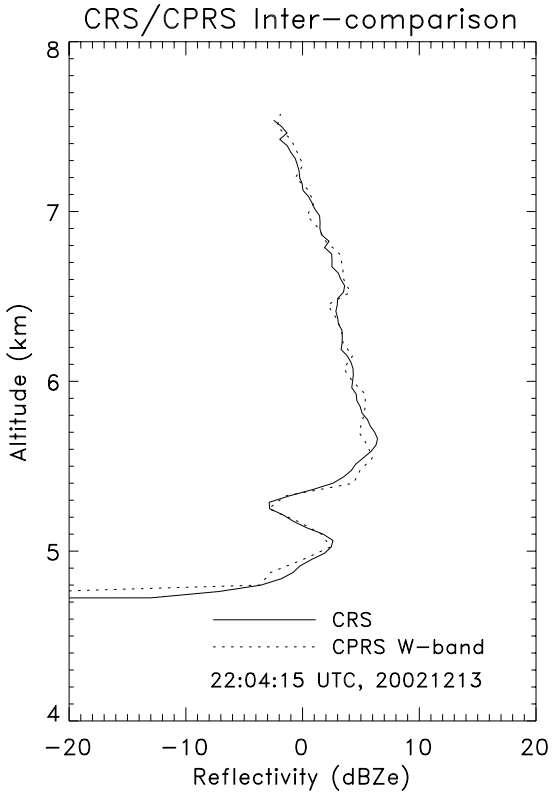

Fig. 1: CRS inter-comparison with CPRS W-band at the University of Massachusetts Amherst, December 13, 2004. The mean difference between two profiles is within 1 dB.

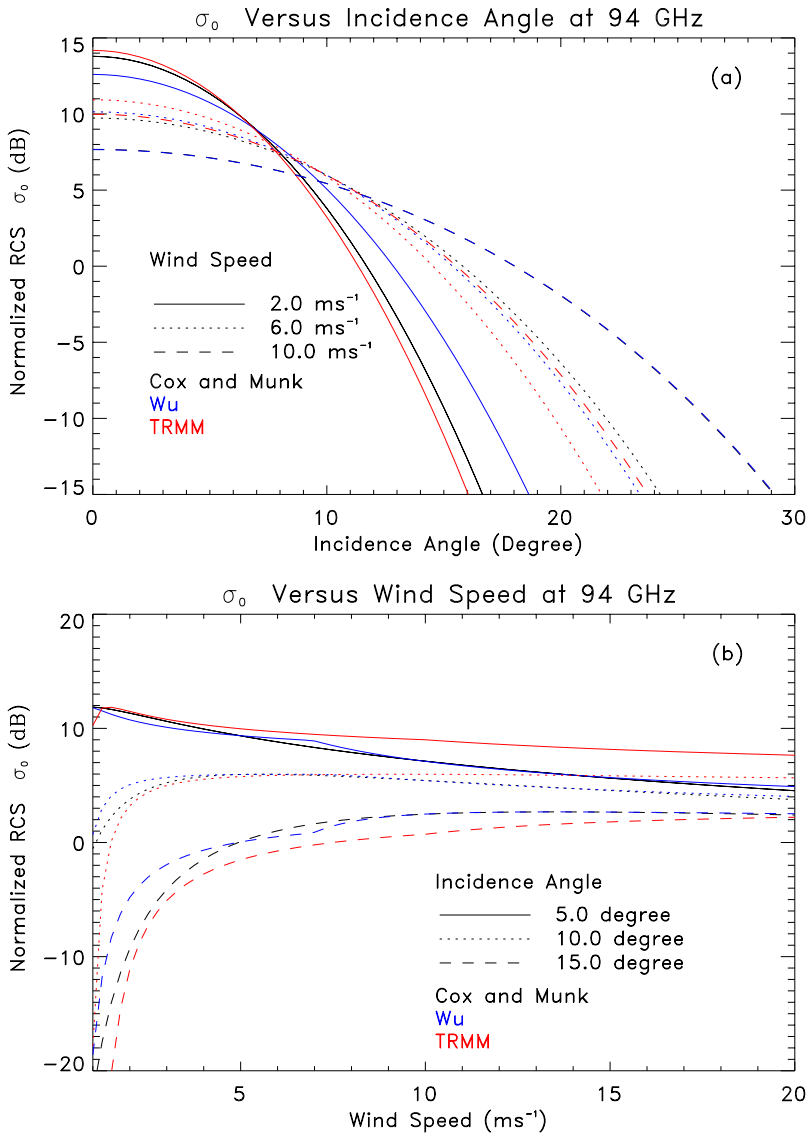

Fig. 2: Ocean surface σ_o versus incidence angle and surface wind speed predicted by the quasi-specular scattering model.

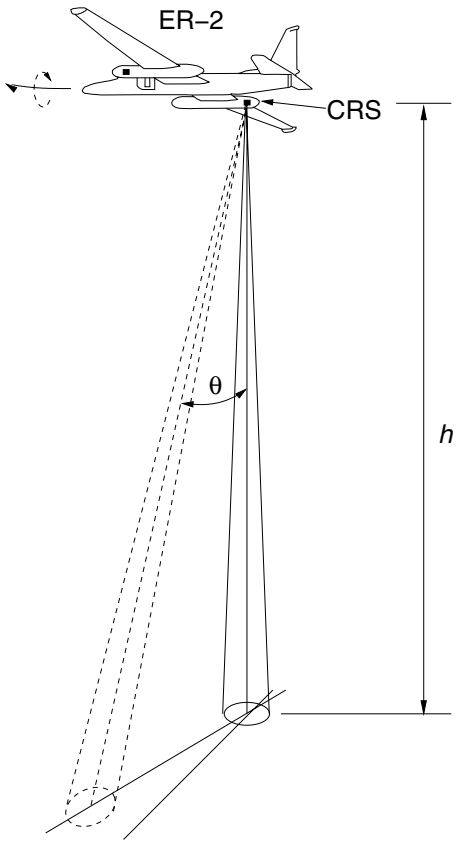

Fig. 3: Geometry of the CRS measurements from NASA ER-2 during the CRYSTAL-FACE experiment. The CRS was installed as nadir looking mode. The radar beam was scanned in a cross-track direction when ER-2 rolled its body to one side during turns.

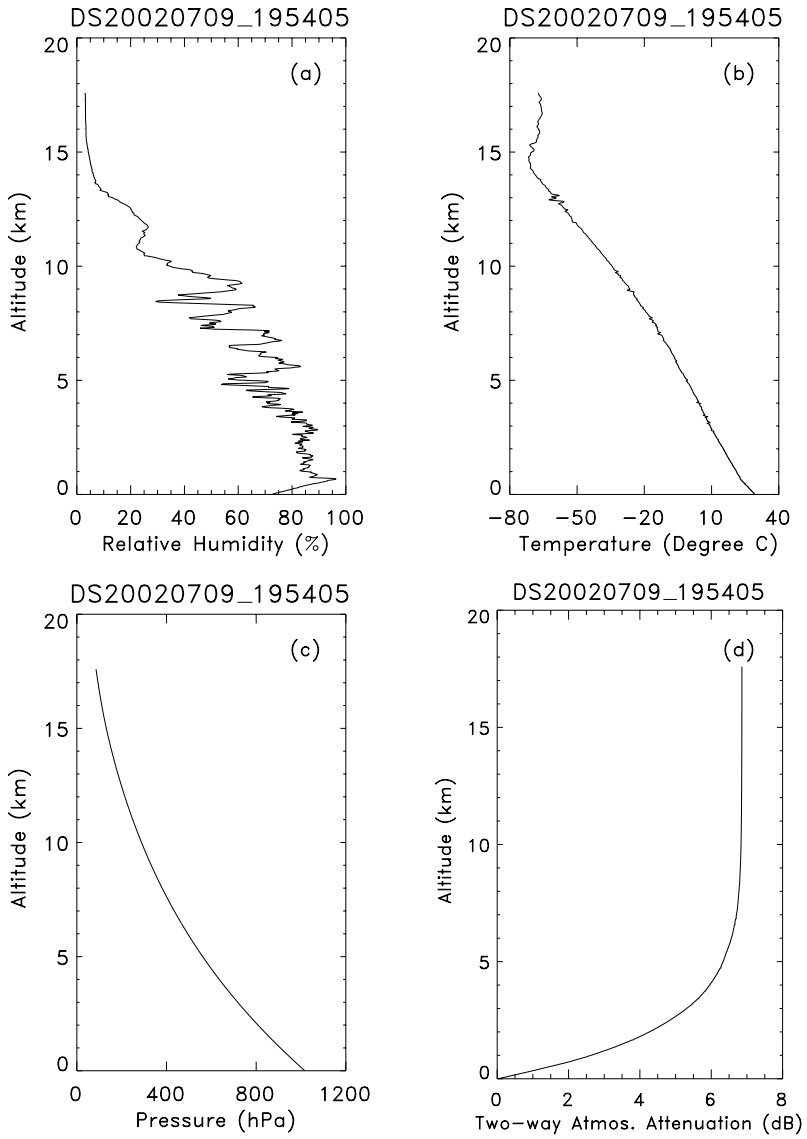

Fig. 4: Dropsonde measurements at 1954 UTC, 9 July, 2002. (a) relative humidity, (b) temperature, (c) pressure. The two-way cumulative path attenuation due to water vapor and oxygen absorption at 94 GHz is shown in (d).

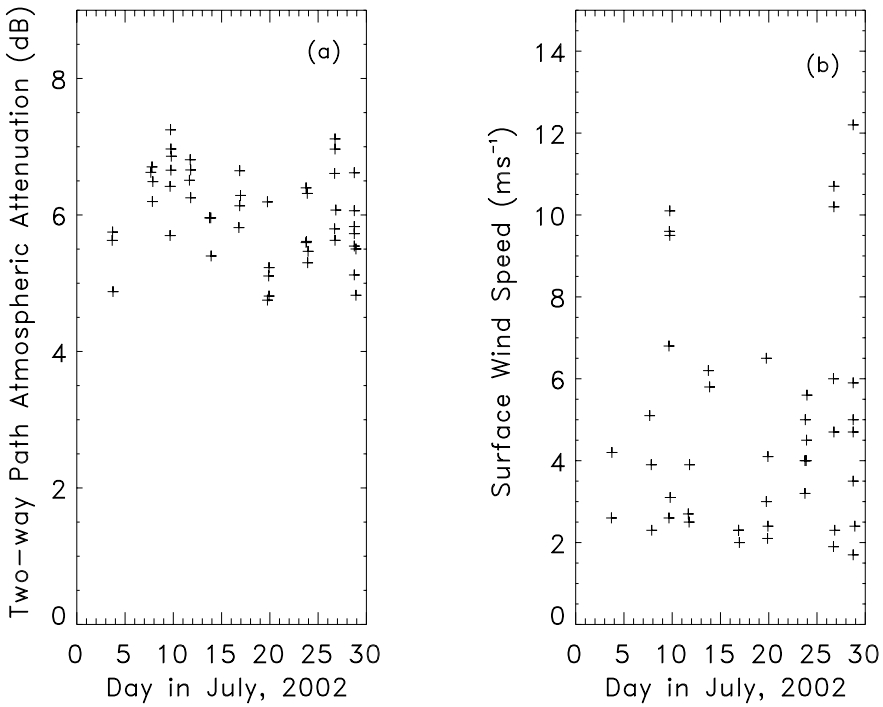

Fig. 5: (a) Two-way path-integrated attenuation due to water vapor and oxygen absorption at 94 GHz derived from dropsonde data collected from CRYSTAL-FACE. It shows the PIAs with a mean of 5.8 dB and a standard deviation of 0.55 dB. (b) Ocean surface wind speed measured by dropsondes during CRYSTAL-FACE.

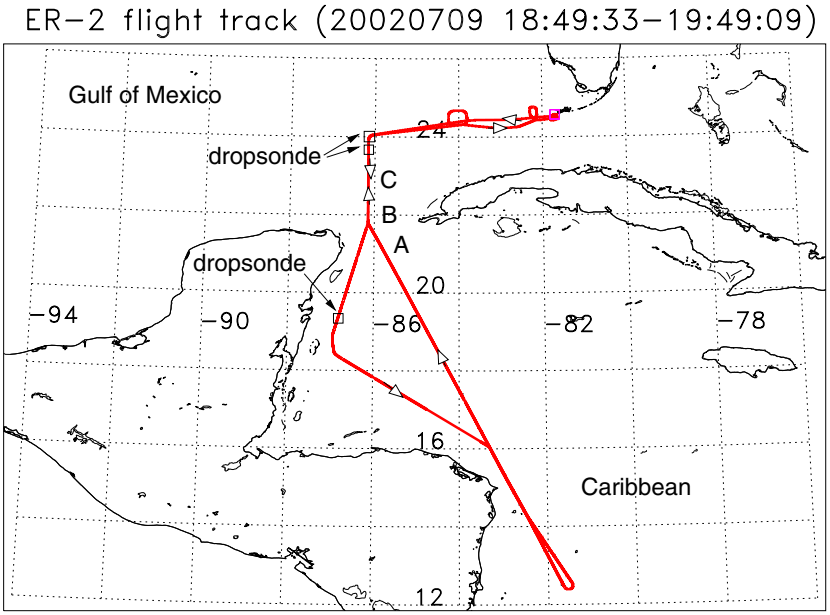

Fig. 6: ER-2 flight track on 9 July 2002. Three dropsonde launch positions near the ER-2 turning point (B) are indicated.

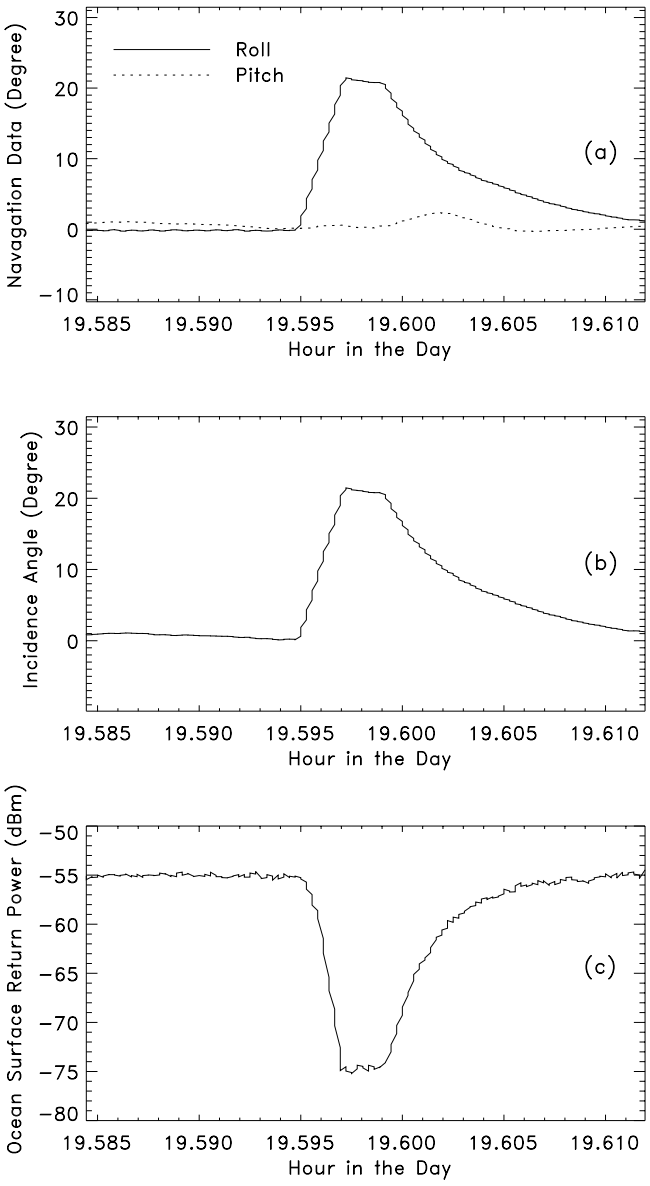

Fig. 7: ER-2 navigational data, radar beam incidence angle and ocean surface return power during the turn through point A, B, and C as shown in Fig. 6.

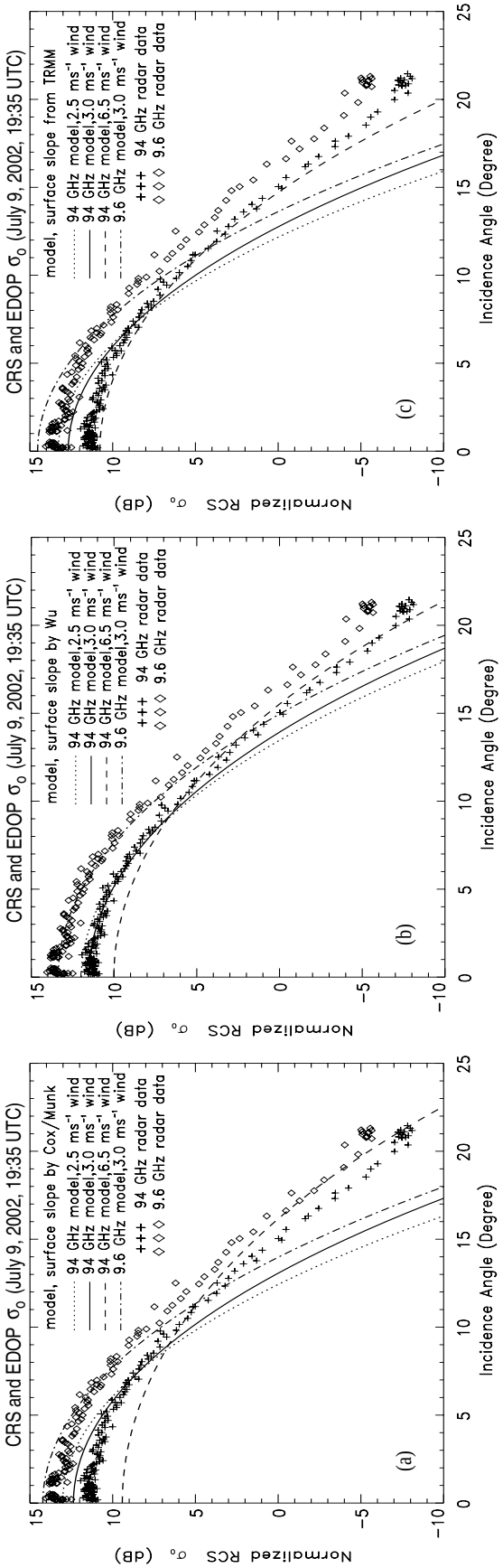
CRS and EDOP σ0 (July 9, 2002, 19:35 UTC)
model, surface slope by Cox/Munk
94 GHz model,2.5 ms-1 wind
94 GHz model,3.0 ms-1 wind
94 GHz model,6.5 ms-1 wind
9.6 GHz model,3.0 ms-1 wind
+++ 94 GHz radar data
◇◇◇ 9.6 GHz radar data
(a)
Normalized RCS σ0 (dB)
Incidence Angle (Degree)
CRS and EDOP σ0 (July 9, 2002, 19:35 UTC)
model, surface slope by Wu
94 GHz model,2.5 ms-1 wind
94 GHz model,3.0 ms-1 wind
94 GHz model,6.5 ms-1 wind
9.6 GHz model,3.0 ms-1 wind
+++ 94 GHz radar data
◇◇◇ 9.6 GHz radar data
(b)
Normalized RCS σ0 (dB)
Incidence Angle (Degree)
CRS and EDOP σ0 (July 9, 2002, 19:35 UTC)
model, surface slope from TRMM
94 GHz model,2.5 ms-1 wind
94 GHz model,3.0 ms-1 wind
94 GHz model,6.5 ms-1 wind
9.6 GHz model,3.0 ms-1 wind
+++ 94 GHz radar data
◇◇◇ 9.6 GHz radar data
(c)
Normalized RCS σ0 (dB)
Incidence Angle (Degree)

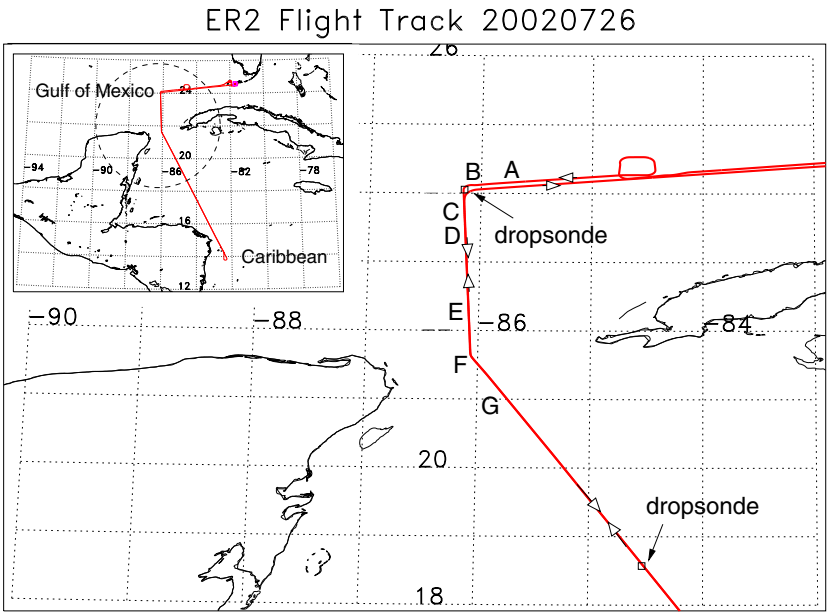

Fig. 9: ER-2 flight track on July 26, 2002. A larger scope plot is shown at the upper left-hand corner. ER-2 flew the track on its outbound trip and on its return trip. It made turns at way points B and F.

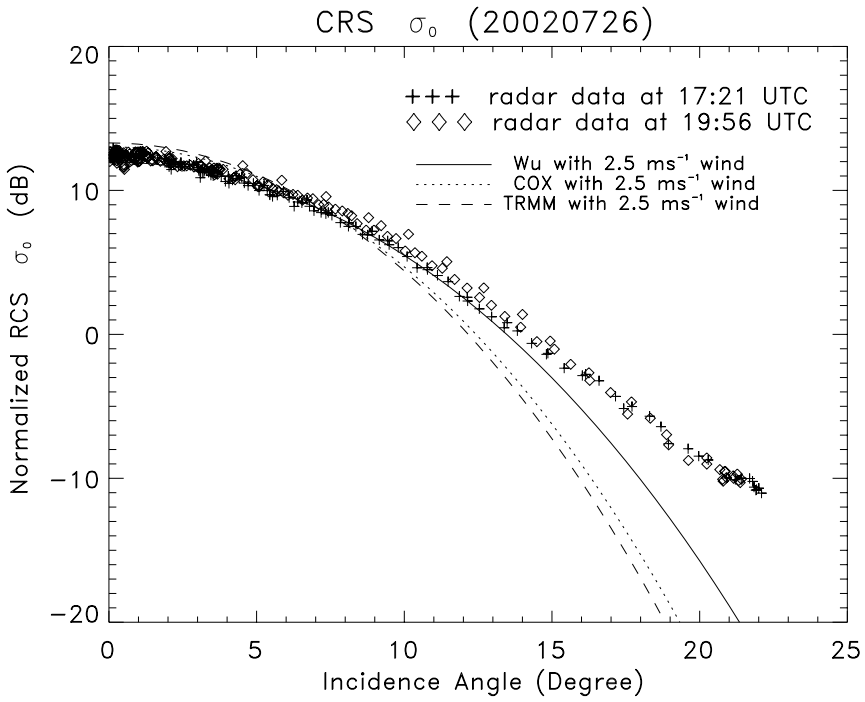

Fig. 10: σ_o measured by CRS versus incidence angle from the turns near way point F shown in Fig. 9. Cross stands for measurements from the outbound turn through E, F, G consequentially. Diamond represents measurements from the turn through G, F, E on the return trip consequentially.

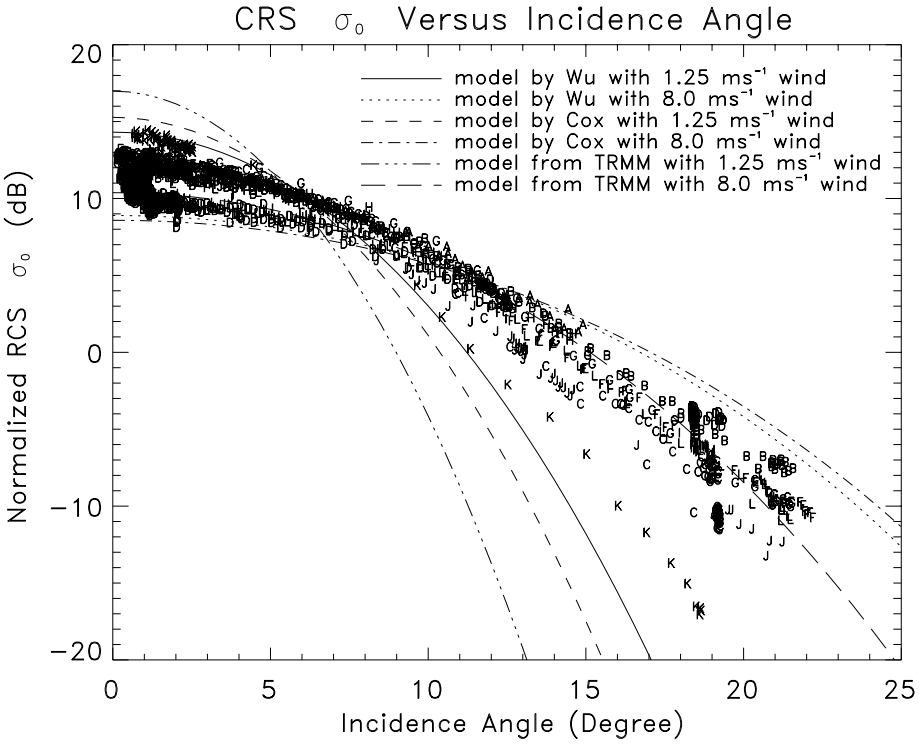

Fig. 11: σ_o measured by CRS versus incidence angle from different days. Twelve turns from clear weather are shown.

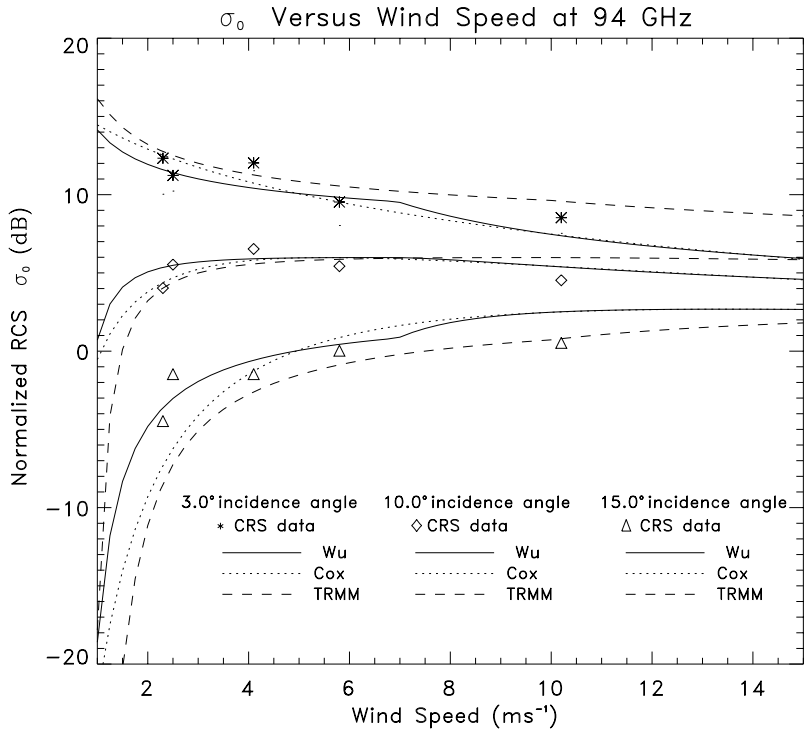

Fig. 12: σ_o versus ocean surface wind speed at different incidence angles. Data points are given by symbols. Results from the quasi-specular scattering model are shown as the solid, dotted and dashed lines.

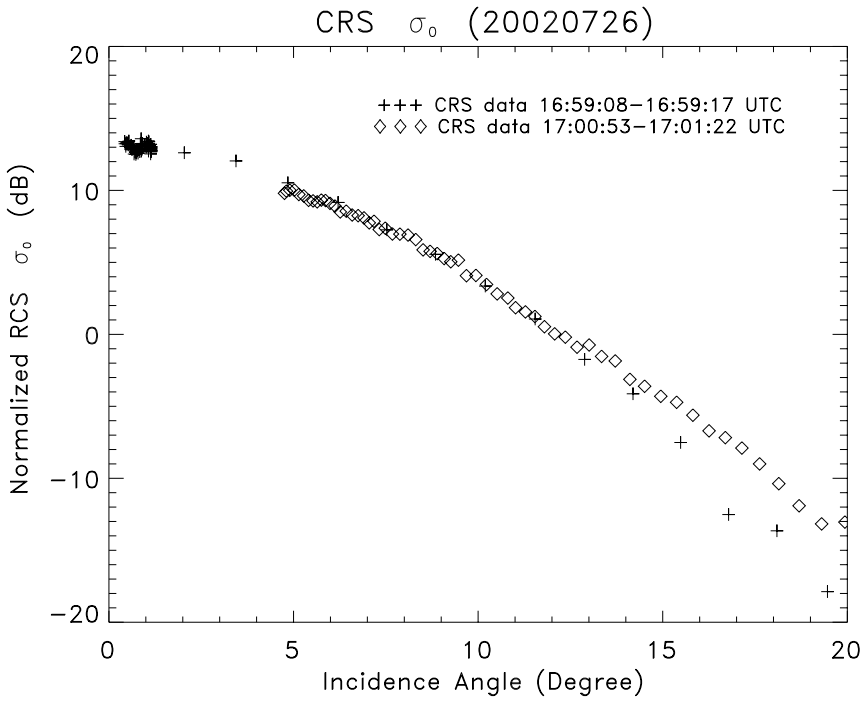

Fig. 13: σ_o from a turn with 100^o heading change. It indicates that σ_o varies relative to wind direction for incidence angle larger than 12^o.

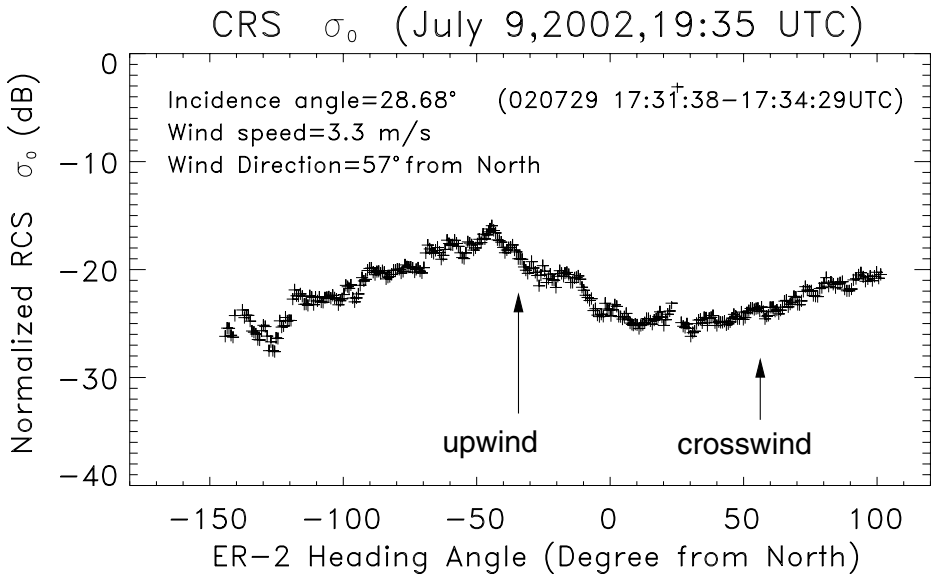

Fig. 14: σ_o versus ER-2 heading angle.

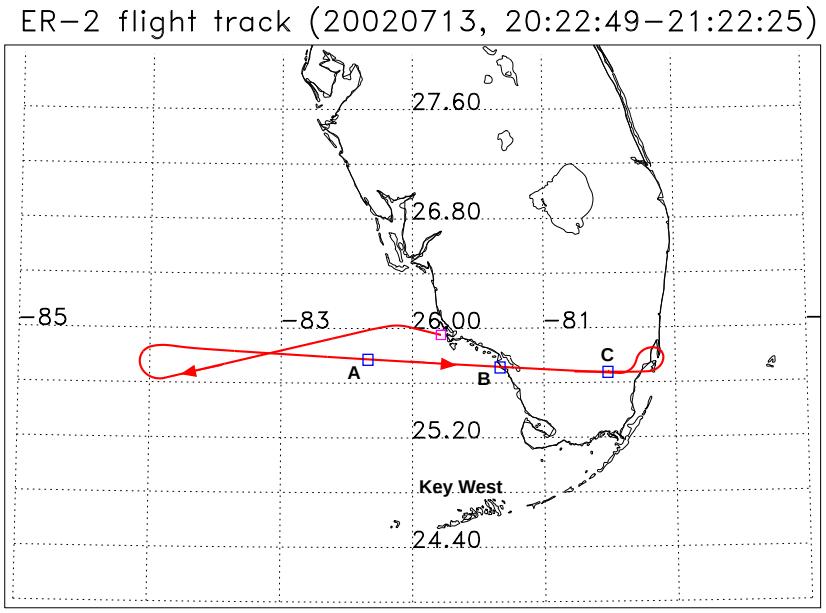

Fig. 15: ER-2 flight track on July 13, 2002. It crossed the coast line at point B (2104:53 UTC)

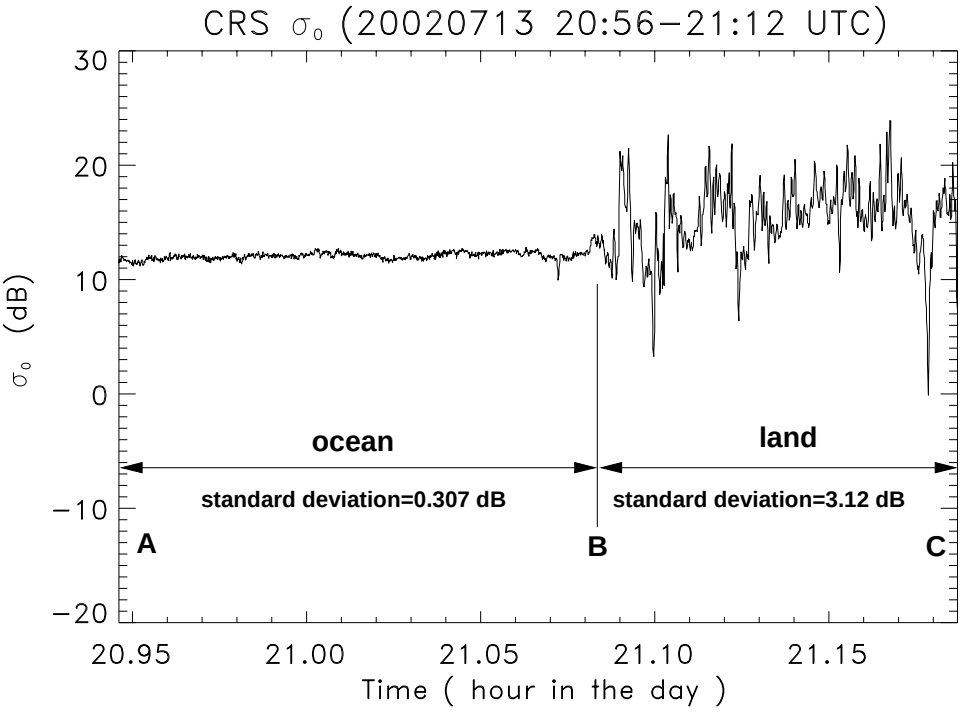

Fig. 16: σ_o measured by CRS from 2056 to 2112 UTC. From the ocean to inland, it shows significant increase in standard deviation of σ_o.